Lab on a Chip

PAPER

View Article Online
View Journal | View Issue

Cite this: *Lab Chip*, 2023, **23**, 2091

Sonoprinting nanoparticles on cellular spheroids *via* surface acoustic waves for enhanced nanotherapeutics delivery†

Reza Rasouli,[a] Radu Alexandru Paun[a] and Maryam Tabrizian *[ab]

Nanotherapeutics, on their path to the target tissues, face numerous physicochemical hindrances that affect their therapeutic efficacy. Physical barriers become more pronounced in pathological tissues, such as solid tumors, where they limit the penetration of nanocarriers into deeper regions, thereby preventing the efficient delivery of drug cargo. To address this challenge, we introduce a novel approach that employs surface acoustic wave (SAW) technology to sonoprint and enhance the delivery of nanoparticles onto and into cell spheroids. Our SAW platform is designed to generate focused and unidirectional acoustic waves for creating vigorous acoustic streaming while promoting Bjerknes forces. The effect of SAW excitation on cell viability, as well as the accumulation and penetration of nanoparticles on human breast cancer (MCF 7) and mouse melanoma (YUMM 1.7) cell spheroids were investigated. The high frequency, low input voltage, and contact-free nature of the proposed SAW system ensured over 92% cell viability for both cell lines after SAW exposure. SAW sonoprinting enhanced the accumulation of 100 nm polystyrene particles on the periphery of the spheroids to near four-fold, while the penetration of nanoparticles into the core regions of the spheroids was improved up to three times. To demonstrate the effectiveness of our SAW platform on the efficacy of nanotherapeutics, the platform was used to deliver nanoliposomes encapsulated with the anti-cancer metal compound copper diethyldithiocarbamate (CuET) to MCF 7 and YUMM 1.7 cell spheroids. A three-fold increase in the cytotoxic activity of the drug was observed in spheroids under the effect of SAW, compared to controls. The capacity of SAW-based devices to be manufactured as minuscule wearable patches can offer highly controllable, localized, and continuous acoustic waves to enhance drug delivery efficiency to target tissues.

Received 15th September 2022,
Accepted 22nd December 2022

DOI: 10.1039/d2lc00854h

rsc.li/loc

Introduction

Nano-mediated drug delivery systems are increasingly explored to reduce off-target toxicity and the immune response by protecting the cargo, transporting high payloads of the active agent, and performing controlled release.[1,2] Despite nanomedicines' success in reducing toxicity, their ability to enhance therapeutic efficacy has been limited in clinical applications.[3,4] One key factor contributing to this limited performance is the poor penetration of nanomedicines into densely packed tissues.[5]

The physical barrier for nanoparticle delivery is exacerbated in pathological tissues, such as tumors, where high interstitial fluid pressure and the overexpression of extracellular matrix impede the convective flow from the circulation to the tumor interstitium. In the absence of convective flow, the diffusion of nanoparticles (NPs) becomes significantly slower and constrained as the size of the nanocarrier increases.[6] This size dependency creates a dilemma as the larger NPs offer the capacity to carry more payloads, but their limited penetration prevents them from realizing better efficacy compared to smaller NPs. For instance, Wang *et al.*[7] showed that 100 nm particles did not offer improved therapeutic efficacy compared to 30 nm particles despite their larger drug cargo.

Given that the majority of the commercially available nanomedicines are within the 100 to 200 nm range,[3] researchers proposed various methods to improve penetration without shrinking the size and payload of NPs. Generally, there are two main approaches to enhance the penetration of nanoparticles: the first strategy focuses on engineering the characteristics of nanoparticles to overcome the diffusion barriers, while the second method is by modulating the tissue or tumor characteristics to facilitate nanoparticle transportation.[8] For instance, the size, surface

[a] *Department of Biomedical Engineering, Faculty of Medicine and Health Sciences, McGill University, Montreal, QC, Canada. E-mail: maryam.tabrizian@mcgill.ca*
[b] *Faculty of Dental Medicine and Oral Health Sciences, McGill University, Montreal, QC, Canada*

† Electronic supplementary information (ESI) available. See DOI: https://doi.org/10.1039/d2lc00854h

chemistry, charge, shape, and mechanical properties of NPs are shown to be influential in their penetration depth into spheroids.[8] Although, the complex engineering of nanoparticles is one part of the equation, the complementary part is the modulation of the tissues' structural barriers and the tumors' physical environment to decompress and reduce physical stresses. One of the methods for stress normalization is to degrade the matrix components, such as collagen.[9] For instance, exposing tumors to extracellular matrix-degrading enzymes, such as collagenase type I, is shown to disrupt the dense interstitial collagen lattices and reduce the intestinal fluid pressure to restore convective flow and enhance the penetration of NPs.[10,11] However, excessive degradation of collagen can make the tumor prone to metastasis and invasion.[8,11,12]

Exogenous forces such as radiation, magnetic, or acoustic forces are commonly explored to modify the physical environment of the tissue.[8] Mechanical forces have been shown to mitigate the tissue barrier for passive diffusion, while their interaction with NPs can also induce active delivery into tumors.[13] Among these mechanical forces, acoustic waves have an extended history of application as means for drug delivery thanks to their label-free and generally non-invasive nature.[14,15] Depending on the actuation conditions and the nature of the target tissue, acoustic waves can create various phenomena such as the hyperthermal effect, cavitation, microstreams, and acoustic radiation forces.[16,17] These acoustic phenomena can lead to various biophysical effects that can enhance the delivery of therapeutics such as sonoporation,[18,19] the loosening and degradation of ECM,[20] the reorganization of intercellular lipids, and increasing cell–cell spacing.[21]

One of the conventional acoustic methods for enhancing nanoparticle delivery is through the hyperthermal effect. The local increase of temperature in tissues can enhance drug delivery by increasing blood circulation and vascular permeability, by reducing intratumoral pressure, or *via* the release of thermosensitive nano-carriers.[16,22,23] The other widely explored ultrasound strategy for drug delivery is cavitation-based delivery, which generally requires nano or microbubbles, such as contrast agents in the target tissue. When the acoustic pressure becomes strong enough, the bubble bursts and releases a shock that induces biophysical effects, such as cell membrane disruption, the opening of intercellular junctions, and altering the tumors' perfusion.[23,24] In several preclinical studies, the potential use of cavitational ultrasound for overcoming the biological drug delivery barriers for tumors and the brain has been investigated.[18,24–26] Roovers *et al.* showed that acoustically activated microbubbles can enhance the deposition and delivery of nanoparticles to spheroids and termed it sonoprinting.[27] Despite their many advantages, the thermal and cavitation effects of conventional ultrasound systems can cause damage to healthy tissues near the tumor depending on their intensity. Blood vessel dilation and damage, oxidative stress, damage to cell structure, and unwanted cavitation can also happen in these ultrasound settings.[22]

In the past few years, Surface Acoustic Waves (SAW) has emerged as a powerful acoustic technology in the biomedical field to circumvent the biocompatibility issues of conventional ultrasound systems by offering high frequency, resolution, and controllability. Recently, SAW was shown to increase the uptake of NPs in adherent cells and improve the non-viral transfection of suspended cells by cavitation-free sonoporation. Acoustic microstreams were the dominant effect in this setting and is also shown the capacity to concentrate bioparticles.[28–30] Moreover, SAW has been used for the trapping and enrichment of NPs on microparticles through inducing interparticle Bjerknes forces.[31]

In this study, we developed an SAW platform to demonstrate the capacity of Eckart microstreams and Bjerknes forces for sonoprinting and delivery of NPs onto spheroids of human breast cancer (MCF 7) and mouse melanoma (YUMM 1.7) cells. We aimed to employ SAW sonoprinting to enhance the delivery of NPs to spheroids without inducing cell damage or a metastatic/migratory phenotype. The proposed platform was designed to generate focused and unidirectional acoustic waves in high-frequency, non-contact, and low input voltage conditions that are proven to minimize mechanical stress and unwanted cavitation. The operation parameters of the SAW device were optimized to maximize Eckart microstreams and Bjerknes forces for sonoprinting and delivery of NPs onto/into melanoma and breast cancer spheroids. To investigate the effect of SAW sonoprinting on the deposition of NPs on spheroids' surfaces, fluorescent polystyrene NPs with the therapeutically relevant size of 100 nm were first employed. Deep confocal microscopy was used to monitor the influence of SAW on the penetration of polystyrene NPs into the deeper layers of spheroids, as well as their spatiotemporal distribution in spheroids' mid-cross-section. To demonstrate the biocompatibility of the SAW platform with cells, both cell viability and the metastatic phenotype of cells were assessed by live/dead assay and gene expression in the presence and absence of SAW. Subsequently, we employed the SAW platform for the delivery of anti-cancer copper diethyldithiocarbamate (CuET)-loaded liposomal NPs to our pseudo-tumor models. The efficacy of the acoustic drug delivery was validated by measuring the cytotoxic effect of CuET-loaded liposomal NPs on spheroids.

Working mechanism of the acoustic platform

To enhance the delivery of NPs into spheroids, we aimed to use acoustic phenomena to achieve two goals: the first aim was to induce the accumulation of NPs on the surface of the spheroids by sonoprinting, and the second step was to increase the penetration of NPs into the inner layers of the spheroids. Our hypothesis was that Eckart streaming and Bjerknes forces can induce the delivery of NPs to the spheroids by transferring vibrational energy to the

suspended particles and creating strong interparticle attraction. Eckart streaming and Bjerknes forces are usually generated in high frequency systems. Therefore, we developed a surface acoustic wave platform that consists of interdigital transducers (IDT) on a piezoelectric lithium niobate (LN) substrate with a high electromechanical coupling coefficient. The working mechanism of such a SAW platform can be described as follows: when radio frequency signals reach the IDT, each finger vibrates to emanate acoustic waves. Positioning the IDT of the same charge on the substrate with a wavelength (λ) distance leads to constructive interference between IDTs to create strong surface acoustic waves. The crystal orientation of the piezo substrate (127.86° *Y*-cut, *X*-propagating) generates a wave-type known as leaky Rayleigh waves, which is suitable for transferring acoustic energy into liquids. We used the leaky nature of Rayleigh waves to guide the acoustic beam from the piezoelectric surface into the glass-bottom Petri-dish *via* a coupling layer of deionized water (Fig. 1A). Once SAW reached the spheroids with NPs in suspension, it creates acoustic streaming flow and acoustic radiation forces, which to our hypothesis, can contribute to the sonoprinting and penetration of NPs in the spheroids (Fig. 1B). The main acoustic streaming flow in the system is attributed to Eckart streaming, which is the result of the viscous attenuation of the acoustic energy during the propagation of waves in the bulk of the fluid.[32] These microstreams not only can bring the spheroids and particles to close vicinity of each other, but are also shown to improve the cellular uptake of NPs.[29]

Upon exposure to SAW, particles scatter a portion of the incident acoustic energy in all directions and create a time-averaged inter-particle acoustic force, known as the secondary Bjerknes force. This force has been recently used to create particle agglomerations, as a method for filtration and enrichment of nanoscale solid particles. Moreover, NPs of hollow structures such as exosomes have been shown to be attracted by Bjerknes forces.[33,34] The intensity of this force is shown to be usually at its peak when the sound wavelength approaches particle diameter ($d/\lambda \approx 0.5$–1).[34,35]

Results and discussion

Optimization of operating parameters for the SAW platform

To ensure the occurrence of Eckart streams and Bjerknes forces for sonoprinting and delivery of NPs to spheroids, we designed the platform to operate at the frequency of 13.7 MHz which is in the range commonly used for high resolution ultrasound imaging, and has a penetration depth of 2–4 cm in soft tissues (see the ESI† for calculation of penetration depth).[36] This frequency corresponds to the wavelength of 300 μm and allows to maximize the Bjerknes forces emitted by the spheroids, which have mean diameters within the 150–300 μm range ($d/\lambda \approx 0.5$–1). For strong Eckart streaming to happen, the chamber dimensions L should be much longer than λ in order to provide enough propagation

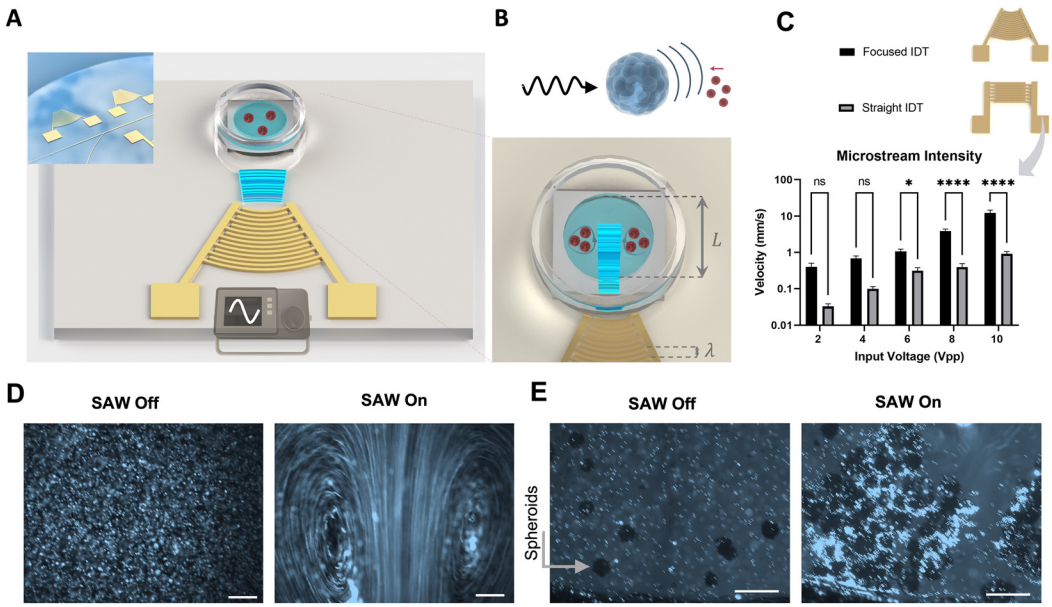

Fig. 1 A) Rendered image of the SAW platform including a piezoelectric substrate with focused interdigitated transducers (FIDT) and a glass-bottom Petri-dish. Upon activation by the function generator, the surface acoustic waves generated by IDTs travel on the substrate surface and leak into the Petri-dish through the coupling layer (water). B) Inside the Petri-dish, acoustic waves propel the media and create acoustic streams which bring the nanoparticles and spheroids at the center of the microstreams to increase the NP uptake. C) Comparison of acoustic microstream intensity produced by straight and focused IDTs. D) Demonstration of Eckart microstreams' formation in the presence of SAW by using fluorescent polystyrene microparticles. E) Suspension of cellular spheroids and microparticles. Upon activation of SAW, spheroids attract the microparticles and increase their concentration in their vicinity. The scale bars are 500 μm. Data is plotted as mean + SD.

path for the acoustic beam to attenuate.[37] The attenuation length of SAW in fluids is frequency-dependent and can be calculated by $x_s = \rho_s c_s \lambda_s / \rho_f c_f$, where ρ_s and ρ_f are the densities of the piezoelectric substrate and fluid, while c_s and c_f are the propagation speed of acoustic waves in the piezoelectric substrate and in fluids, respectively.[38] Laying these parameters in the above equation, the attenuation length for our SAW platform with the operating wavelength of 300 μm approximates to 3.86 mm. Hence, the well diameter of L = 1 cm is used in the proposed set-up to provide sufficient attenuation path for the acoustic waves and the formation of strong Eckart streams.

The next design criterion was the IDT configuration for creating traveling SAW. Straight IDTs are the standard setting for SAW while focused IDTs (FIDT) allow concentrating the acoustic energy in a confined domain. For producing Eckart streams with straight IDT, the chamber should be placed at the edge of the IDT to induce heterogeneous exposure of the fluid to acoustic waves. This non-uniformity of acoustic field becomes very sensitive to the positing of the chamber in each experiment, and also leads to asymmetric vortices.[39,40] In contrast, the focused IDTs' design could inherently produce a spatial gradient of acoustic pressure in a highly localized region and create symmetrical acoustic vortices with maximum unidirectional acoustic momentum.[41,42] To quantify the microstream intensity produced by these two designs (straight IDT and focused IDTs), particle streak velocimetry was performed at different input voltages by using fluorescently labeled polystyrene particles of 5 μm for better visualization, as tracking of NP trajectory was barely possible in low magnifications and large domains.[43,44] Fig. 1C shows that the microstreaming from the focused IDT design is approximately 10 times faster than that of the straight IDTs. This is in agreement with the literature reporting that the use of focused IDT can minimize reflective standing waves, which tend to suppress acoustic streams.[29,38] Moreover, Zhong *et al.* showed in a recent study that focused IDT can transmit around 4.83 fold more acoustic energy compared to straight IDT, where acoustic waves propagate bi-directionally causing energy loss.[45] Fig. 1D displays the counter-rotating acoustic microstreams from a focused IDT source. In the absence of acoustic energy, particles remained quiescent. As expected, upon the introduction of acoustic waves to the suspension, the acoustic beam propelled the liquid in the propagation direction, creating a time-averaged fluid jet. This jet flow in a confined chamber induces a backflow to develop counter rotational Eckart vortices. The Eckart vortices span throughout the chamber and can be rapidly generated and stopped by controlling the radiofrequency signals (Video S1†).[37] To observe the interaction of the acoustic phenomena and microparticles with spheroids, coherent YUMM 1.7 spheroids were cultured in a U-bottom 96-well for 24 hours, followed by resuspension and incubation for 2 days on a shaking plate. When YUMM 1.7 spheroids were introduced to the microparticle suspension, and were exposed to the SAW waves from the focused IDT source, the hydrodynamic forces gathered the spheroids in the vortexes while bombarding them with the microparticles. As a result, after only a few seconds of acoustic energy activation, the fluorescent microparticles were surrounding the spheroids, denoting the effectiveness of our acoustic platform in enhancing the exposure of spheroids to the particles (Fig. 1E). This accumulation of particles around the spheroids was an indication of the presence of the attractive Bjerknes forces to induce sonoprinting.[31] Moreover, the vigorous acoustic streams that were observable in our SAW platform, suggested the optimal working parameters for NP penetration for the next set of experiments. The acoustic streams have been shown to be the main phenomena for delivering acoustic energy to suspended particles for cellular uptake.[28,29] Since the Bjerknes forces decay by the square of the particle distance, the microstream can also enhance the Bjerknes forces by bringing the spheroids and microparticles into the immediate vicinity of each other. As shown in Video S2,† the drag forces from acoustic streams gathered the spheroids and microparticles in the vortex center, while the convective mass transfer by the streams ensured the close contact and homogenous exposure of microparticles to the spheroids.

Cell spheroids' exposure to SAW does not affect cell viability

To investigate the impact of acoustic radiation forces and the hydrodynamic forces generated by acoustic streams on cells' viability, coherent and viable spheroids of MCF 7, in addition to YUMM 1.7, were formed. Both these cell lines can readily form spheroids in culture and their native occurrence location in the body is rather accessible to acoustic stimulations. Therefore, bioinert SAW devices can be conceptually employed as skin patches to potentially complement the treatment of skin cancer, such as in-transit or unresectable cutaneous melanoma.[46,47] MCF 7 spheroids were formed using the shaking plate method with a spinning speed of 80–90 rpm. The spheroids of both cell types were cultivated after 3 days and characterized. The MCF 7 spheroids indicated a slightly larger mean diameter (278.7 ± 50.8 μm) compared to that of YUMM 1.7 (234.7 ± 48.1 μm), while YUMM 1.7 spheroids showed slightly more roundness (Fig. 2A). The size of both spheroids was within the peak Bjerknes forces in the device. Furthermore, as a common indicator of the cell–cell compactness in spheroids,[48] the optical density measurement revealed a higher density in YUMM 1.7 (Fig. 2A).

Fig. 2B and C show the MCF 7 and YUMM 1.7 spheroids for 1, 3, 5, 10, and 15 minutes SAW exposure and control, stained with green Calcein AM as a live cell marker, red ethidium homodimer III for dead cells, and blue Hoechst

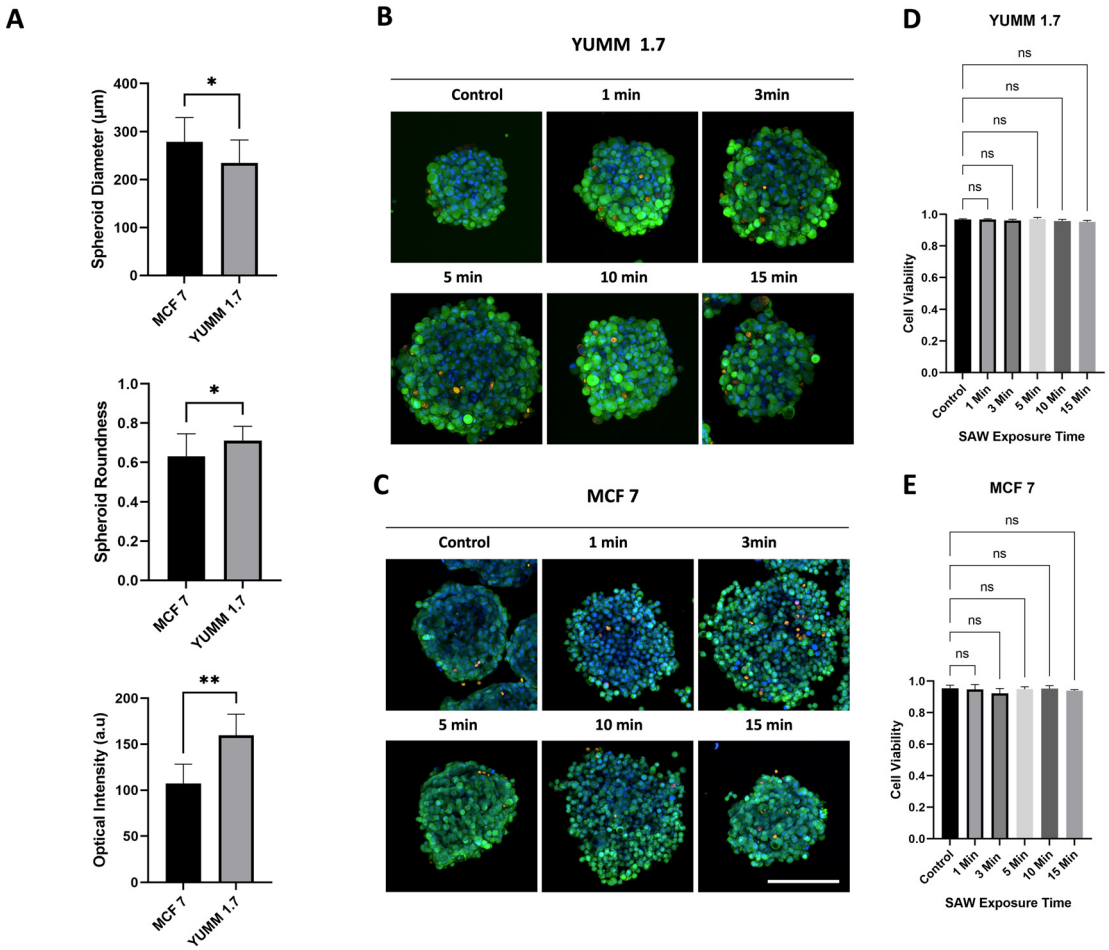

Fig. 2 A) The morphological characterization of MCF 7 and YUMM 1.7 spheroids, including the diameter, roundness, and optical intensity. The cell viability in the B) YUMM 1.7 spheroids and C) MCF 7 spheroids after different exposure times to 10 Vpp SAW. Spheroids were stained with green Calcein AM for live cells, orange ethidium homodimer III for dead cells, and Hoechst 33342 for nuclei. The figures show the maximum projection of the planes at a *Z* distance of 10 μm, acquired by high-resolution confocal microscopy. Scale bar is 200 μm. The quantification of cell viability is performed using the Harmony 4.9 software for D) YUMM 1.7 and E) MCF 7. Data is plotted as mean + SD.

33342 for nuclei. To quantify the cell viability in spheroids after SAW exposure, the total number of cells and dead cells were counted in 3D and plotted in Fig. 2D and E. The results indicated no significant effect of SAW on cell viability, regardless of the duration of their exposure to SAW. The SAW post-exposure cell viability was over 95% and 92% for YUMM 1.7 cell spheroids and MCF 7 cell spheroids, respectively. These numbers are considerably higher compared to conventional acoustic treatments such as cavitational methods with common cell viability as low as 60%.[21] The high rates of cell viability in our SAW platform are in agreement with the literature, which ascribe the inherent biocompatibility of SAW to the high operation frequency that suppresses the possibility of destructive cavitation and ensures minimal stress on the cells.[28] The negligible effect of SAW streaming and radiation forces on cell viability has made this technology even compatible with spheroid formation.[49,50] Moreover, the low driving voltage of 10 Vpp with the contactless setting of our acoustic platform reduce heat generation, often harmful to cells.[51] Accordingly, 10 min SAW exposure time and a 10 Vpp excitation voltage were used for the following experiments to ensure cell viability.

SAW allows for sonoprinting NPs onto spheroids' surfaces

After confirming the presence of the SAW-mediated microstreams and microparticle accumulation on the spheroids, the capacity of the system for sonoprinting NPs on the spheroids was investigated. Reducing the size of particles from the microscale to the nanoscale can theoretically boost sonoprinting since the drag forces from acoustic streaming become more dominant over other suppressive acoustic phenomena, such as primary radiation forces.[28,52] This is due to the linear relationship of the microstreams' Stokes forces with the diameter of particles (d), while standing radiation forces are proportional to d^3. As a result, when the diameter of particles decreases from micro to nano, the primary radiation forces decrease faster.[39]

To fathom and quantify the effect of SAW exposure on the accumulation of NPs on spheroids, fluorescently

labeled 100 nm polystyrene NPs with carboxylic acid (COOH) on the surface were employed. The caveats for choosing these NPs were to isolate the effect of SAW on NPs accumulation from other effects, such as nonspecific adsorption or size that might interfere with our measurements.[10] Negatively charged carboxylated NPs were thus purposely chosen to minimize the non-specific adsorption to cell membrane components and to facilitate NPs diffusion into the spheroids' core regions.[10] The rationality for choosing 100 nm diameter particles was based on the fact that most anticancer nanomedicines have a diameter in this range. This NP size is reported to allow for an optimal cargo loading capacity while being within the efficient nano delivery size range (between renal clearance and upper EPR fenestration sizes).[3] Sonoprinting of these polystyrene NPs onto YUMM 1.7 and MCF 7 spheroids was then examined using the SAW platform. To better represent the total NP accumulation on the spheroids, the maximum intensity projection of the spheroids treated with 5 μg mL^{-1} polystyrene NPs was acquired by confocal microscopy and depicted in 2D (Fig. 3A). Predictably, as the spheroid exposure time to NPs increased from 3 min to 15 min, a higher concentration of NPs was attached to the spheroids' surface for both cell types, regardless of the application of SAW (Fig. 3B and C). Nevertheless, at each time point, the presence of SAW significantly enhanced both the distribution and the density of NPs on the spheroids compared to control spheroids (NSAW). In

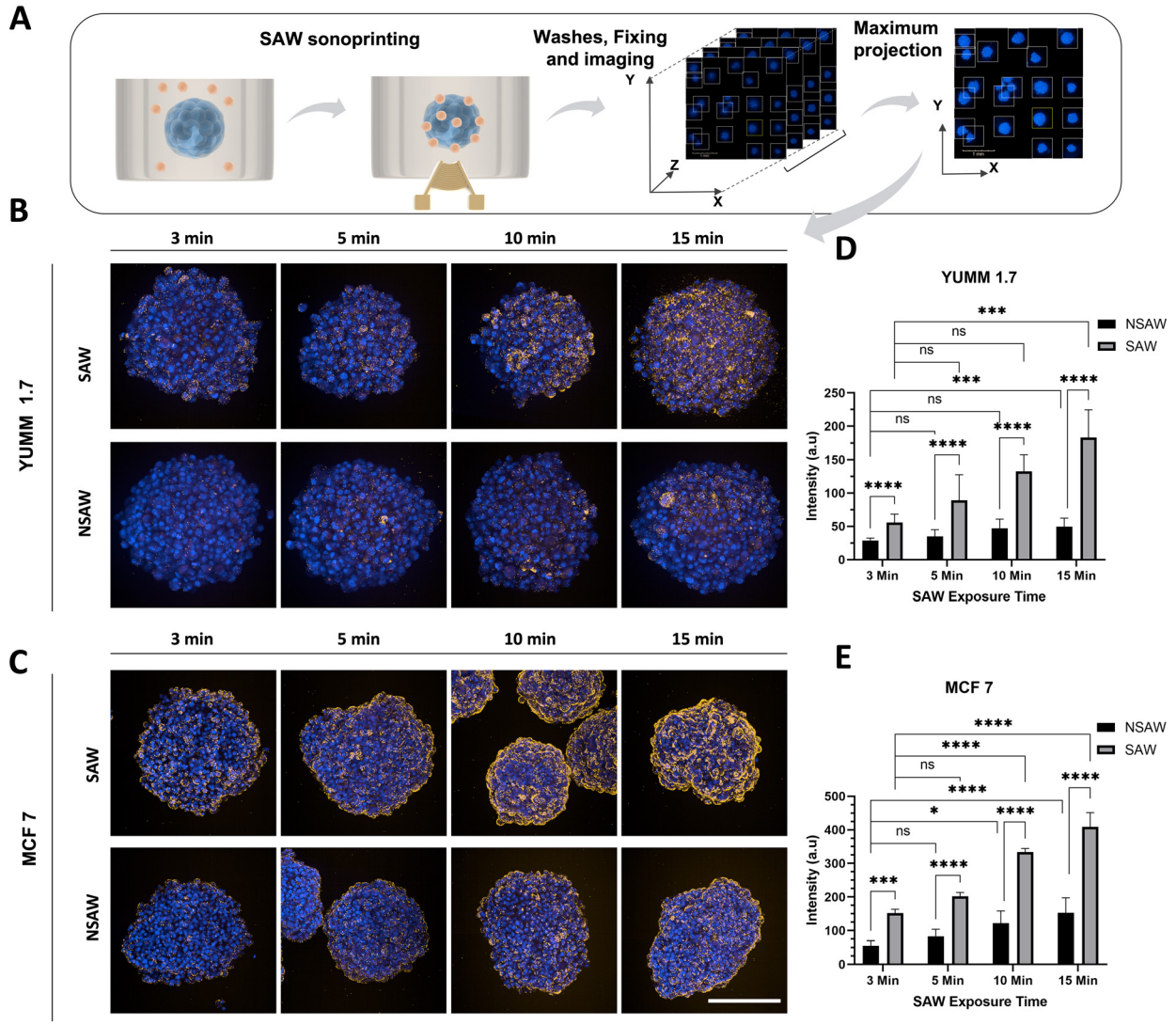

Fig. 3 A) Overview of the SAW-mediated sonoprinting experiments and analysis. Accumulation of the 100 nm polystyrene nanoparticles (orange) on spheroids of B) YUMM 1.7 and C) MCF 7 cells in the presence (SAW) and absence (NSAW) of acoustic waves with different exposure times. The cells' nuclei were stained with blue Hoechst 33342. The figures show the maximum intensity projection of the planes acquired by water-immersed, high-resolution confocal microscopy. Scale bar is 200 μm. The fluorescent intensity of the nanoparticles was measured and quantified in graph D) for YUMM 1.7 and E) for MCF 7. Data is plotted as mean + SD.

addition, the application of SAW allowed for a more homogenous distribution of NPs on the spheroids. This can be attributed to the acoustic microstreams shown in Video S2,† which constantly rotate spheroids and transport NPs, exposing the entire spheroids' interfaces uniformly to NPs. The more noticeable impact of the

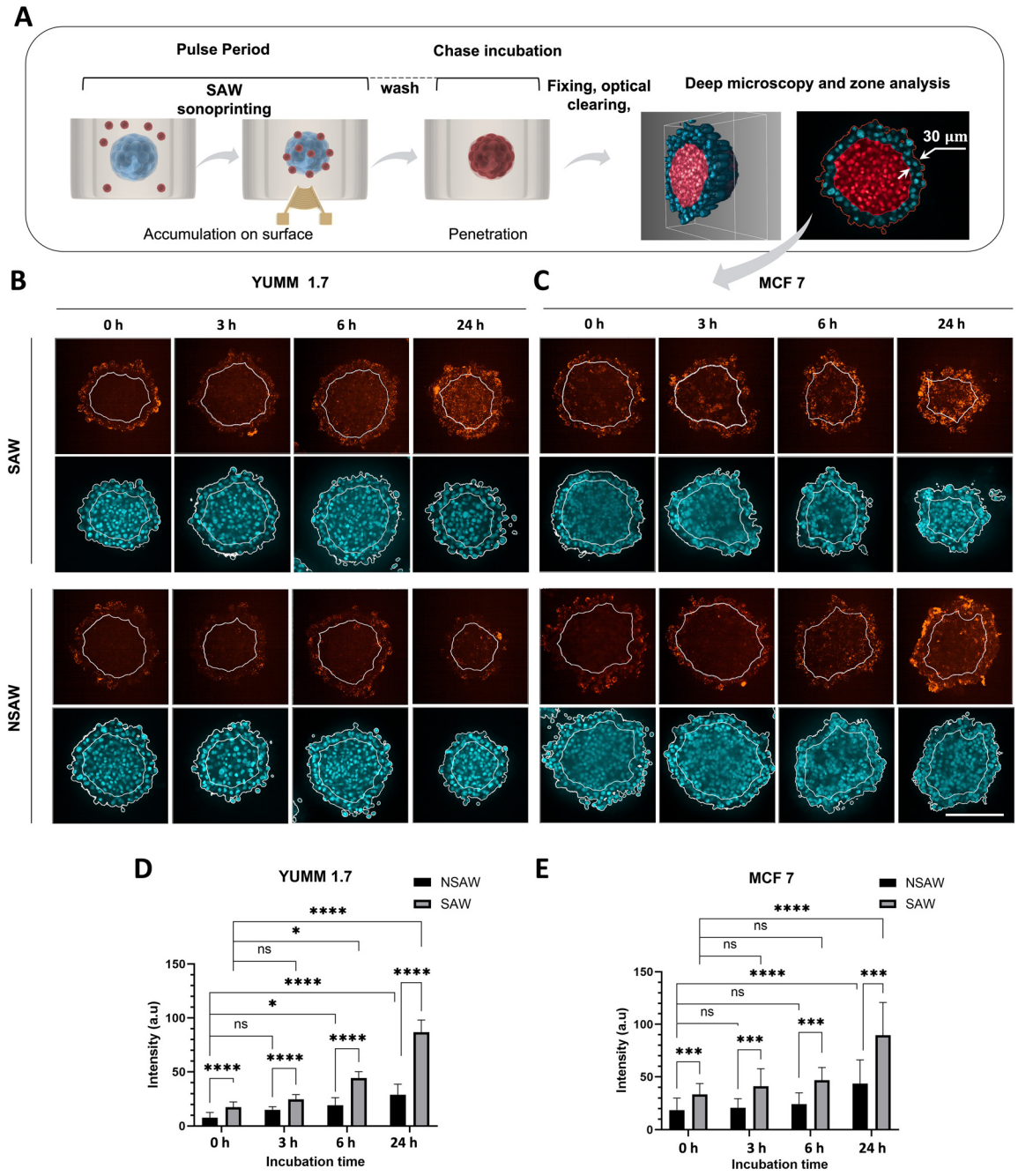

Fig. 4 A) The experiment sketch for the nanoparticle transport assay, deep confocal microscopy, and zone analysis of spheroids. After the transport assay, the spheroids are fixed and cleared. The mid cross-section of spheroids are imaged and divided into two zones of total and core zones delineated by white boundaries. The distribution of the 100 nm polystyrene nanoparticles (red) after different chase times, in the spheroids of B) YUMM 1.7 and C) MCF 7 spheroids with (SAW) and without (NSAW) acoustic waves. The figures show the mid cross-section of the spheroids in the red channel for nanoparticles (top) and the cyan channel for cells' nuclei stained with Hoechst 33342 (bottom) acquired by water- immersed confocal microscopy. In the cyan channel, the outer line shows the boundary of the spheroids defined by the nuclei, and the inner line (the same line in red channel) shows the core zone of the spheroids with a 30 μm margin from the spheroid's boundary. Scale bar is 200 μm. D) and E) show the intensity of the nanoparticles that penetrated into the core region of YUMM 1.7 and MCF 7 spheroids respectively, quantified by image analysis of spheroids' cross-sections. Data plotted as mean + SD.

SAW, however, was the increase in the number of NPs accumulated onto the spheroids.

In order to quantify the NP concentration, the average fluorescent intensity of the NPs within the spheroid's boundary was measured. As depicted in Fig. 3D and E, for all the time points, when SAW was applied, the intensity of NPs was significantly higher. The mean NP accumulation was increased up to 2.7-fold for MCF 7 spheroids and approximately 3.7 times for YUMM 1.7 after 15 min exposure to SAW, compared to that of spheroids without the application of SAW. Interestingly, the intensity of accumulated NPs was substantially less in YUMM 1.7 compared to that of MCF 7 cell lines. This can be due to the more compact structure of YUMM 1.7 spheroids as revealed by the measurement of their optical density (Fig. 2A).

SAW increases the delivery of NPs into the core of cell spheroids

Although NPs in the range of 100 nm in diameter present the optimal size, their therapeutic effects for the treatment of solid tumors have so far been limited due to their low penetration into the core of the tumor.[7] To analyze the dynamics of polystyrene nanoparticle penetration into our pseudo-tumor model, and their spatiotemporal distribution following their exposure to SAW, we conducted a NP transport assay using the pulse-chase procedure[53] followed by 3D deep imaging and zonal analysis of the spheroids.

The pulse-chase procedure included a 10 min treatment of spheroids with 5 μg mL^{-1} FluoSpheres NPs in serum-free media to enable uptake (pulse time) with and without SAW activation. The spheroids were then washed and translocated to a fresh medium to remove suspended NPs and stop the uptake. After the pulse treatment, the spheroids were incubated for 0, 3, 6 and 24 hours for investigating the NP penetration pattern throughout the spheroid's layers over time (chase time). Analysis of the spatiotemporal distribution of NPs in the spheroids necessitated deep and high-resolution imaging of the spheroids' inner layers (Fig. 4A). To enhance the visualization of the spheroids' core, optical clearance was performed, which is shown to increase the light transmission depth by reducing the scattering and absorption in the spheroids.[54]

Fig. 4B and C show the NPs distributions at the middle cross-section of MCF 7 and YUMM 1.7 cell spheroids respectively, acquired by water-immersion confocal microscopy. Immediately after NP treatment (chase time = 0 h), the accumulation of NPs was restricted to the peripheries of the spheroids. However, in the presence of SAW, some NP spots could be detected in the inner layers of MCF 7 spheroids, while compact YUMM 1.7 spheroids do not reveal a significant increase of fluorescence intensity in the core. As the chase time progresses, the NPs gradually migrate from the outermost layers into the inner layers for both spheroid types. The rate of this translocation seems to be strongly influenced by their exposure to SAW. In the absence of the SAW, the NP distribution shows dominant peripheral localization even at the 24 hours chase time point. SAW exposure considerably increased the penetration of the NPs into the inner layers and the fluorescence was distributed more uniformly throughout the spheroids. To quantify the SAW impact on the penetration of NPs into the core, we defined two image zones using the Harmony software (-Fig. 4A, right). The outer boundary line defines the boundary of the spheroids in the Hoechst 33342 channel. To omit the NP stuck on the periphery of the spheroids from the penetration measurements, we defined a core region with a distance of 30 μm from the spheroid's boundary. The fluorescent intensity of NPs in the core region was measured for different incubation times and subtracted from the control (Fig. 4D and E). The SAW activation increased the intensity of NPs in the core region by approximately two times for MCF 7 while the surge was almost threefold for YUMM 1.7 spheroids after 24 hours of incubation.

The higher trafficking of the nanoparticles in the core of spheroids treated with SAW can be due to the reorganization of the cellular membrane and cell junctions,[21] as well as the increased deposition of nanoparticles onto spheroids by exposure to SAW. This is in agreement with the considerably higher penetration of NP in MCF 7 cell spheroids compared to YUMM 1.7 cell spheroids, which showed higher NP uptake in the sonoprinting test, as well as their less compact structure compared to that of YUMM 1.7. Given that the compactness of the spheroids and therefore the penetration of NPs is significantly influenced by ECM, further studies are necessary to investigate the performance of the SAW delivery in co-culture models and spheroids with ECM-depositing fibroblasts where the ECM is more abundant. Moreover, the ECM composition and concentration, the mechanical characteristics of the components such as collagen and their network mesh size, the mechanism of compaction, and the presence of different integrins and cadherins that govern cell junctions can significantly influence the extent of nanoparticle penetration into tissues,[55–57] and ultimately impact the functionality of the SAW systems as suggested by the difference of results in the two cell types discussed above.

SAW increases the efficacy of anticancer drug-loaded nanoliposomes delivery into spheroids

Demonstrating that the surface acoustic waves actuation leads to nanoparticle sonoprinting onto, and higher trafficking into cell spheroids, as a proof-of-concept study, we investigated the capacity of the SAW technique to deliver nanotherapeutics to MCF 7 and YUMM 1.7 spheroids as pseudo-tumor models. To this end, nanoliposomes

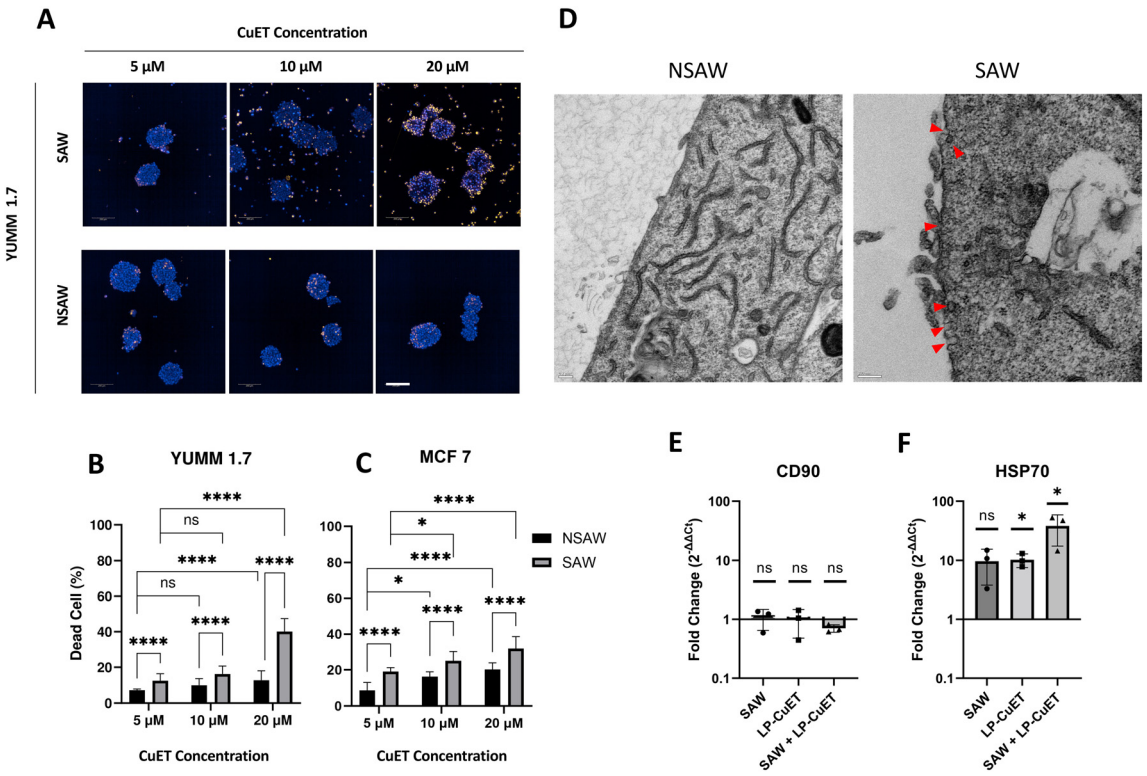

Fig. 5 A) The anti-cancer activity of liposomal CuET nanoparticles with different concentrations, with and without acoustic waves. The dead cells are stained by orange ethidium homodimer III, while blue Hoechst 33342 shows the nuclei of total cells. More dissociated cells and less compact structure are observable with the exposure of SAW, especially at higher concentration. The figures are the maximum projection of confocal planes, and the scale bar is 200 μm. B) and C) show the percentage of dead cells over total number of cells for YUMM 1.7 and MCF 7 spheroids, respectively. Data is plotted as mean + SD. D) TEM micrographs showing the presence of caveolae (red arrows) in SAW-treated YUMM 1.7 compared to NSAW control. Scale bar is 200 nm. E) and F) RT-qPCR results of *CD90* and *HSP70* genes with YUMM 1.7 cell spheroids exposed to 10 min SAW alone (SAW), 10 μM of LP-CuET NPs, and the combination of SAW and LP-CuET NPs for 10 min. The results are normalized to NSAW, and the data is plotted as mean ± SD, and the statistical analysis is performed using ΔCt values (Fig. S2†).

encapsulating the CuET metal complex (LP-CuET) were used. CuET is a promising drug candidate for cancer therapy that causes cancer cell death by blocking the p97-NPL4 pathway leading to the accumulation of misfolded proteins and a heat shock response.[58]

Nanoliposomes are used to carry CuET, as the drug is not soluble in aqueous media, such as body fluids.[59]

Since the nanoliposomal CuET formulation might prevent the penetration of CuET into the deep layers of tumors, and potentially limit its efficacy, we used our SAW platform to overcome the physical and cellular barriers of LP-CuET delivery. Both cell spheroids were exposed to 5, 10, and 20 μM LP-CuET with a mean size of 110.7 ± 1.0 nm (Fig. S1†) for 10 minutes in the presence or absence of SAW. The spheroids were then washed and immediately moved to fresh media.

Fig. 5A shows the viability of spheroids after a 6 hours chase incubation. As the concentration of LP-CuET increases, more dead cells can be detected in the NSAW group; however, the percentage of dead cells remained small even at 20 μM, since the spheroids were exposed to LP-CuET for just 10 minutes and then moved to fresh media immediately after. In the SAW group, on the other hand, the shift in the number of dead cells, as well as their structure was more noticeable, particularly at the periphery of the spheroids. Moreover, the disintegration of the spheroid structure was evident by the number of cells detached from spheroids and dispersed in the wells with increasing concentration of LP-CuET. Both the cell detachment and death were the result of the SAW-mediated delivery, which suggest higher accumulation of the nanoliposomes and deeper penetration, only after 10 minutes of spheroid exposure to SAW. The effect of SAW on the cytotoxic efficacy of LP-CuET in YUMM 1.7 and MCF 7 spheroids are shown in Fig. 5B and C. For any concentrations of LP-CuET, the anticancer activity was boosted with SAW exposure. A 55% increase in the number of MCF 7 dead cells and near a threefold increase for YUMM 1.7 spheroids could be noted at 20 μM LP-CuET concentration. This result shows the SAW can increase the sensitivity of YUMM 1.7 spheroids to LP-CuET, which is interesting given that 2D cultured YUMM 1.7 cells are slightly less sensitive to CuET than MCF 7 cells (Fig. S1†).

To ensure that the increase in the cytotoxicity was caused by the efficient delivery of liposomal CuET, and not the mere bombardment of the nanoparticles by SAW, a group of YUMM 1.7 spheroids were treated with empty liposomes and SAW in the same experimental condition. The results showed

no significant surge in cell death between the group treated with empty liposomes + SAW and that of the control group without liposomes or SAW (Fig. S6†), confirming the cytotoxic effect was due to the more efficient delivery of the CuET component.

Moreover, transmission electron microscopy (TEM) images showed a large increase in the number of heavily stained membrane folds and cavities in YUMM 1.7 cells after SAW treatment compared to NSAW controls that are consistent with caveolar structures (Fig. 5D). These structures were not present in multiple NSAW spheroids (Fig. S4†), whereas they were consistently observed in SAW spheroids (Fig. S5†). Research has shown that cells that are under constant mechanical stress, such as in the endothelium, adapt to the environmental stress by upregulating the number of caveolar structures on the plasma membrane to improve their stretchability.[60–62] The caveolar structures observed in our melanoma model seem to be part of the cellular adaptation to acoustic stress, which likely contributes to the increased nanoparticle uptake, as membrane folds play an important role in clathrin-independent endocytosis.[63–65] Complementary to caveolar structures, some SAW-treated cells show membrane regions that have bilayer discontinuity and shedding, which could be due to the formation of pores, however, artifacts from the TEM processing cannot be ruled out (Fig. S5†). Additional research must be performed to confirm our findings that acoustic stress can indeed upregulate the formation of membrane folds and/or caveolae in cells, and further elucidate how these changes affect nanoparticle uptake in cell and tissue models. If these findings can be recapitulated, the SAW platform could offer a biocompatible alternative to enhance the uptake and delivery of nanocarriers and subsequently, increase the efficiency of nano-mediated drug delivery and transfection processes.

SAW improves CuET-loaded nanoparticle cytotoxicity but does not induce a cell migration phenotype

Higher risk of migratory behavior associated with metastasis is frequently reported in other modulation methods, such as tumor collagenase treatment,[8,11,12] which in fact has a comparable performance to our SAW platform in terms of penetration increase of ≈3-fold for the 100 nm carboxylated polystyrene beads.[10] To investigate whether SAW has a similar effect on the spheroids' phenotype, we measured the expression of the *CD90* gene as a surrogate marker for metastatic behaviour, as higher *CD90* expression is associated with a migratory metastatic phenotype in melanoma.[66] *CD90* is also an active regulator of cell–cell adhesion in various cancer types involved in cell migration.[67–69]

RT-qPCR results showed no change in *CD90* expression in the YUMM 1.7 cell spheroids after SAW exposure or upon LP-CuET treatment suggesting there is no significant difference occurring in the mechanics of YUMM 1.7 cell motility in these conditions (Fig. 5E). Interestingly, when spheroids were treated with both LP-CuET and SAW, there was an apparent but non-significant decrease in *CD90* expression (0.706-fold decrease). This trend seems consistent with previous literature findings considering that endoplasmic reticulum stress, which is caused by LP-CuET, is associated with the downregulation of *CD90* expression.[70] A limitation of this assay, however, was that affected cells could detach from the spheroid surface upon cytotoxic LP-CuET/SAW treatment (Fig. 5A), which could be lost during the process of mRNA isolation and purification, resulting in an experimental bias towards the cells in the core of the spheroid. Additionally, more robust experiments need to be performed to evaluate the migration and invasion potential of cancer cells post-SAW treatment. The expression *HSP70* was also measured (Fig. 5F), since *HSP70* is known to be upregulated during CuET-induced heat shock, as *HSP70* is a protein chaperone that is essential for cellular homeostasis during proteotoxic stress.[58,71] We observed a significant upregulation of *HSP70* during treatment with LP-CuET alone (~10-fold increase, p = 0.0102) and a similar nonsignificant upregulation of *HSP70* (~10-fold increase, p = 0.0747) upon exposure of YUMM 1.7 spheroids to SAW. The upregulation of *HSP70* during SAW treatment alone could be due to localized vibrational and acoustic energy on the cells. The combinatory effect of LP-CuET and SAW, however, was drastically larger (near 40-fold increase, p = 0.0136), suggesting a marked increase in proteotoxic stress in the spheroids and thereby the effective delivery of the drug-loaded NPs. While the increase in *HSP70* from NSAW control samples was not statistically significant in the SAW group alone, there was a clear trend towards more cellular stress as cells were exposed to acoustic energy but without any significant changes in cytotoxicity when LP-CuET was absent. Taken together, the data suggest that SAW improves NP sonoprinting, penetration and delivery into cancer cell spheroids leading to more pronounced efficacy in the presence of cytotoxic nanoparticles.

Conclusion

In this work, we introduced an SAW platform to enhance the delivery of NPs to 3D pseudo-tumors of breast cancer MCF 7 and melanoma YUMM 1.7 spheroids. The proposed surface acoustic waves-based platform was fabricated on a lithium niobate substrate with focused interdigital transducers and activated with 10 Vpp driving voltage, allowing for the generation of acoustic microstreams and Bjerknes forces that induce the convective transport and aggregation of the nanoparticles in the cell spheroids. The SAW sonoprinting led to a significant increase in the accumulation of NPs onto, as well as significantly more trafficking of NPs into the inner layers of cell spheroids. The SAW platform was evaluated for its ability to improve the delivery of anticancer nanotherapeutics to spheroids using liposomal CuET nanoparticles. The presence of SAW caused higher cell death, indicating enhanced drug delivery efficacy. Moreover, while higher concentrations of the drug could be delivered to the pseudo-tumor, the RT-qPCR results for YUMM 1.7 cell

spheroids showed no significant increase in a metastatic phenotype of the spheroids. Although the *in vivo* effects of SAW-assisted drug delivery should be thoroughly explored, the efficient nanotherapeutic delivery results shown in this study coupled with the wide range of bioinert and wearable materials compatible with this technology open the venue for the development of exciting biomedical devices, such as skin patches to enhance drug delivery by administering localized, continuous, and controllable acoustic waves. Moreover, the low voltage and biocompatible nature of the SAW technology present enormous opportunities to enhance the penetration and delivery of nanoparticles to 3D spheroids for *in vitro* applications, such as nanoparticle-based gene editing of spheroids and organoids as building blocks for tissue engineering, which is of use for guided differentiation of organoids.[72–76]

Materials and methods

Materials

127.86° *Y*-cut, *X*-Propagating SAW grade Lithium Niobate wafers (4-inch diameter) were acquired from Precision Micro-Optics (Massachusetts, USA). MatTek 35 mm glass-bottom Petri dish #1.5 coverslip, Dulbecco's Modified Eagle Medium (DMEM/F1) fetal bovine serum (FBS), penicillin–streptomycin (P/S), formaldehyde solution, Invitrogen NucBlue™ Live ReadyProbes Reagent (Hoechst 33342) and orange/red fluorescently labeled 100 nm polystyrene carboxylated NPs (FluoSpheres, cat. no. F8800 Molecular Probes, Oregon) were purchased from Thermo Fisher Scientific, Canada. 96 Well glass bottom plate with high-performance #1.5 cover glass was acquired from Cellvis, USA. Tissue optical clearing reagent Scaleview-S4 was acquired from FUJIFILM Wako Pure Chemical Corporation, USA.

Device fabrication and setup. The focused IDTs design was used to restrict and concentrate the acoustic energy to the confined domain in the well. Each IDT had the thickness of 75 μm with the same gap size between the fingers, corresponding to the wavelength of λ = 300 μm.

The SAW substrate was fabricated by standard soft-lithography and e-beam evaporation. A 500 μm, double-sided polished 127.86° lithium niobate piezoelectric wafer was coated by 10 μm-thick photoresist layers (S1813, MicroChem, Texas, USA) with the bake time, spin speed and lithography dosage per the manufacturer protocol. After developing the pattern, a 10 nm titanium adhesion layer and 100 nm gold layer was deposited on the substrate, using an E-beam evaporator (BJD1800, Airco Temescal, California, USA). The sacrificial S1813 was peeled off by sonication in Microposit MF319 developer, at 70 °C to develop the interdigitated transducers.

For operating the platform, IDTs were connected to a function generator (AFG3011C, Tektronix, USA) and were activated by squared radiofrequency (RF) signals at their optimum frequency, which is determined by IDT design and their wavelength (λ = 300 μm, correspond to the frequency of $f \approx$ 13.7 MHz). The acoustic waves were transported from the piezoelectric substrate to the glass bottom Petri dish (MatTek) using DI water as the coupling layer. A total of four SAW devices were made for this study.

Cell culture. The mouse melanoma cell line (YUMM 1.7) was obtained from Ian Watson, and human breast adenocarcinoma cells (MCF 7) were purchased from the American Type Culture Collection (ATCC, Rockville, MD). Both cell lines were cultured in Dulbecco's modified Eagle medium (DMEM) with 10% FBS and 1% penicillin/streptomycin (GIBCO). YUMM 1.7 cell media also contained 1% non-esstential amino acids (GIBCO). The cells were cultured in T75 cell flasks and were suspended using 0.25% (w/v) Trypsin prior to spheroid formation.

Spheroid formation. For MCF 7 spheroids' formation, the suspended cells were transferred to low attachment Petri-dish. The Petri dish carrying suspended MCF 7 cells were then transferred to a shaker plate in the incubator with a spinning speed of 80–90 rpm. The cells naturally form spheroids and after 3 days they were harvested for the NP delivery tests. To produce YUMM 1.7 spheroids, trypsinized and suspended cells were transferred to a 96-well, non-treated, U-shaped-bottom microplate. After 24 hours, the multiple spheroids were formed in each well, and to detach them from the plate, each well was pipetted multiple times. The suspended spheroids were then moved to a low adhesion Petri-dish which was placed on a shaker plate in the incubator for 2 additional days prior to the NP delivery tests.

NP transport assay in spheroids. After 3 days in culture, spheroids were washed with PBS, followed by a 15 minutes serum starvation in DMEM in the incubator at 37 °C. Fluorescently tagged 100 nm polystyrene carboxylated NPs were diluted in serum-free DMEM medium. After serum starvation, spheroids were transferred to the glass bottom petri dish and NPs were added to the spheroids to reach the final volume of 160 μL. For nanoparticle accumulation and penetration tests, fluorescently tagged 100 nm polystyrene carboxylated were diluted in serum-free DMEM medium to reach the final concentration of 5 μg mL^{-1}, which approximately corresponds to a particle concentration of 9×10^9 particles per ml. According to the manufacturer, FluoSpheres nanoparticles were produced by incorporating the fluorescent dye within the bead's polystyrene matrix. Compared to the surface conjugation, this method offers better trapping dye molecules and protecting them from leakage into surrounding media. This was critical in the NP penetration experiments to ensure the proper monitoring of NP diffusion into spheroids.

For the anticancer drug delivery test, liposomal CuET was added to reach the final concentration of 5, 10, and 20 μM which corresponds to approximately 2.3×10^9 particles per ml for the lowest concentration to 9.5×10^9 particles per ml for the highest concentration according to the NTA data. NP treatment for the NSAW groups involved 10 minutes incubation of spheroids with the abovementioned

concentrations for each test, followed by two washing steps with PBS. For the SAW experiments, a drop of water was placed on the piezoelectric substrate as the coupling layer and the Petri-dish was mounted on the drop. The glass well of the Petri-dish, where the spheroid and NPs were present, was carefully aligned on top of the IDT. Upon activation with 10 Vpp driving voltage (corresponding to the power of 0.175 W) and the frequency of 13.7 MHz, the IDT generated visible Eckart streams in the middle of the glass well. After 10 min SAW exposure, the spheroids were washed two times with PBS followed by either incubation or fixing depending on the follow-up experiments. For each experiment, at least 15 spheroids were measured and quantified in each group to assure reproducibility.

Live/dead cell evaluation. The viability assays were performed by the live/dead kit (Viability/Cytotoxicity Assay Kit, Biotium, USA). Spheroids were washed with PBS and stained green with 2 μM Calcein AM for live cells and red with 4 μM ethidium homodimer-III for dead cells. Hoechst 33342 was used per manufacturer's protocol to stain the cells' nuclei.

For empty liposomes with SAW group, spheroids were treated with the same liposome formulation used for drug delivery, albeit without CuET encapsulation. Spheroids were exposed to SAW for 10 min. For each experiment, at least 17 spheroids were measured and quantified in each group to assure reproducibility.

Sample preparations for imaging. After the nanoparticle treatments, spheroids were washed twice with PBS before fixing in 4% (v/v) paraformaldehyde for 30 min. Clearing solution Scaleview S4, which is compatible with well plates, was added to the spheroid prior to the imaging to enhance light penetration depth. Incubating spheroids in the clearing agent at 37 °C overnight allowed the clearing agent to homogenize the light refractive indices in the 3D sample and improve signal detection in the inner layers of the spheroids.[77,78] Pictures were acquired using confocal mode on Opera Phenix™ high-content screening system (Perkin Elmer) equipped with microlens-enhanced spinning disk. For the penetration and accumulation studies, spheroids were imaged by water immersion objectives in order to acquire higher image quality in *z*-direction.[77]

Image analysis. Particle streak velocimetry technique was employed for quantitative analysis of microstreams, using 5-micron polystyrene particles. The displacement (Δ) of particles by microstreams was measured at various exposure times (τ) with imageJ to calculate the velocity.

The total number of cells was counted in 3D where the z-stack from confocal microscopy (Opera Phenix™ high-content screening system) was used to reconstruct the spheroids in 3D and the "Find Nuclei" module of the Harmony® 4.9 software was used to count the total number of cells in each plane in the Hoechst 33342 channel. To detect the dead cells, "Find Cell" in the ethidium homodimer channel was used. For zone analysis of the spheroids, the "Find region" and resized region modules of the software was used. The physical characteristics of the spheroids were measured using Harmony® 4.9 imaging and analysis software. The "Find region" module was used to detect the boundaries of the spheroids for the size and roundness analysis. The roundness was calculated by = $4\pi \times [\text{area}]/[\text{perimeter}]^2$ and the effective diameter was measured by $D_{\text{eff}} = (2 \times [\text{area}]/\pi)^{1/2}$.

Liposomal CuET synthesis. CuET encapsulation was performed using the ethanol injection method, as previously described.[59] Briefly, phospholipids, cholesterol, and CuET were dissolved in 100% ethanol and heated to 50 °C. The solution was then rapidly injected into ultrapure water to yield liposomal CuET. The ethanol was removed by rotary evaporation and the solution was filtered using a 0.22 μm membrane, suspended in 1x PBS and stored at 4 °C.

Transmission electron microscopy. SAW-treated and NSAW control YUMM 1.7 spheroids were fixed using 3% glutaraldehyde in PBS overnight and embedded in a 4% low-melting agarose gel the next day. The agarose gel was trimmed, and the embedded spheroids were stained with 1% OsO_4 in 1.5% potassium ferricyanide before dehydration using a series of acetone in water (30%, 50%, 70%, 80%, 90%, 3× 100% with 10 minutes incubation for each series). The samples were then further embedded using a series of EPON™ resin in acetone (50%, 66%, 75%, 100% with at least 6 hours incubation time) followed by polymerization at 60 °C for 48 hours. The samples were cut into ultrathin sections using an ultramicrotome, transferred onto copper grids, and counterstained with uranyl acetate and lead acetate before imaging with the FEI Tecnai G2 Spirit Twin 120 kV microscope.

RNA isolation and RT-qPCR. YUMM 1.7 spheroids were divided into four groups: LP-CuET treated (10 μM, for 10 minutes) with and without SAW, SAW without LP-CuET (10 minutes), and no SAW (NSAW) control group. Spheroids were then washed and incubated for 6 h in serum-free media prior to RNA extraction. Total RNA was extracted using TRIzol™ and the PureLink® RNA mini kit. RNA quality was evaluated by NanoDrop™ One C, and one-step RT-qPCR was performed using the Luna® Universal One-Step RT-qPCR kit according to manufacturer instructions. Fold change in gene expression was calculated using the $2^{-\Delta\Delta Ct}$ method using GAPDH as a housekeeping gene and normalized to NSAW controls. The following primers were used (Table 1):

Table 1 Primer information for RT-qPCR

Gene	Forward (5′-3′)	Reverse (5′-3′)
GAPDH	CCCTTAAGAGGGATGCTTTCAAGT	ACTGTGCCGTTGAATTTGCC
CD90	CTAAGTCCGTGCAGGAAGGG	CACACTCCAGAGGCTTGGTT
HSP70	GAAGGTGCTGGACAAGTGC	GCCAGCAGAGGCCTCTAATC

Statistical analysis

All experiments were performed independently with a minimum of 3 replicates. One-way analysis of variance (ANOVA) was applied for comparison of three or more group means using the Tukey test, and student's regular t test was used to assess the statistical significance between the SAW treated and untreated (NSAW) groups. For RT-qPCR results, Dunnett's 3T correction was carried out. The data were then plotted using GraphPad Prism (GraphPad software, San Diego, CA, USA) and were considered significant when $p < 0.05$ (* < 0.05, ** < 0.05, *** < 0.005, **** < 0.0001).

Conflicts of interest

There are no conflicts to declare.

Acknowledgements

The authors would like to acknowledge Natural Science and Engineering Council of Canada for their financial support through Discovery Grant and CREATE in Continuous Flow Synthesis. The authors would also like to thank the McGill Facility for Electron Microscopy Research (FEMR) and Michael Yitayew for their help with sample preparation for TEM. The authors are greatful to Ian Watson for providing the melanoma cell line used in this study.

References

1 X. Chen, F. Jia, Y. Li, Y. Deng, Y. Huang and W. Liu, *et al.*, Nitric oxide-induced stromal depletion for improved nanoparticle penetration in pancreatic cancer treatment, *Biomaterials*, 2020, **246**, 119999.
2 E. Blanco, H. Shen and M. Ferrari, Principles of nanoparticle design for overcoming biological barriers to drug delivery, *Nat. Biotechnol.*, 2015, **33**(9), 941–951.
3 Y. Zhu, Y. Song, Z. Cao, L. Dong, Y. Lu, X. Yang and J. Wang, Magnetically Actuated Active Deep Tumor Penetration of Deformable Large Nanocarriers for Enhanced Cancer Therapy, *Adv. Funct. Mater.*, 2021, **31**(35), 2103655.
4 M. E. R. O'Brien, N. Wigler, M. Inbar, R. Rosso, E. Grischke and A. Santoro, *et al.*, Reduced cardiotoxicity and comparable efficacy in a phase IIItrial of pegylated liposomal doxorubicin HCl(CAELYX™/Doxil®) versus conventional doxorubicin forfirst-line treatment of metastatic breast cancer, *Ann. Oncol.*, 2004, **15**(3), 440–449.
5 G. M. Cooper, *The Development and Causes of Cancer*, 2000.
6 J. W. Nichols and Y. H. Bae, Odyssey of a cancer nanoparticle: From injection site to site of action, *Nano Today*, 2012, **7**(6), 606–618.
7 J. Wang, W. Mao, L. L. Lock, J. Tang, M. Sui and W. Sun, *et al.*, The Role of Micelle Size in Tumor Accumulation, Penetration, and Treatment, *ACS Nano*, 2015, **9**(7), 7195–7206.
8 J. Ding, J. Chen, L. Gao, Z. Jiang, Y. Zhang and M. Li, *et al.*, Engineered nanomedicines with enhanced tumor penetration, *Nano Today*, 2019, **29**, 100800.
9 V. P. Chauhan and R. K. Jain, Strategies for advancing cancer nanomedicine, *Nat. Mater.*, 2013, **12**(11), 958.
10 T. T. Goodman, P. L. Olive and S. H. Pun, Increased nanoparticle penetration in collagenase-treated multicellular spheroids, *Int. J. Nanomed.*, 2007, **2**(2), 265–274.
11 M. Magzoub, S. Jin and A. S. Verkman, Enhanced macromolecule diffusion deep in tumors after enzymatic digestion of extracellular matrix collagen and its associated proteoglycan decorin, *FASEB J.*, 2008, **22**(1), 276–284.
12 L. Zhang, Y. Wang, Y. Yang, Y. Liu, S. Ruan and Q. Zhang, *et al.* High Tumor Penetration of Paclitaxel Loaded pH Sensitive Cleavable Liposomes by Depletion of Tumor Collagen I in Breast Cancer, *ACS Appl. Mater. Interfaces*, 2015, **7**(18), 9691–9701.
13 S. Barua and S. Mitragotri, Science Direct Challenges associated with penetration of nanoparticles across cell and tissue barriers: A review of current status and future prospects, *Nano Today*, 2014, **9**, 223–243.
14 S. Mitragotri, Devices for overcoming biological barriers: The use of physical forces to disrupt the barriers, *Adv. Drug Delivery Rev.*, 2013, **65**, 100–103.
15 S. Barua and S. Mitragotri, Challenges associated with penetration of nanoparticles across cell and tissue barriers: A review of current status and future prospects, *Nano Today*, 2014, **9**, 223–243.
16 K. D. Watson, C.-Y. Lai, S. Qin, D. E. Kruse, Y.-C. Lin and J. W. Seo, *et al.*, Ultrasound Increases Nanoparticle Delivery by Reducing Intratumoral Pressure and Increasing Transport in Epithelial and Epithelial–Mesenchymal Transition Tumors, *Cancer Res.*, 2012, **72**(6), 1485–1493.
17 D. Dalecki, Mechanical bioeffects of ultrasound, *Annu. Rev. Biomed. Eng.*, 2004, **6**, 229–248.
18 S. Snipstad, S. Hanstad, A. Bjørkøy, Ý. Mørch and C. de Lange Davies, Sonoporation using nanoparticle-loaded microbubbles increases cellular uptake of nanoparticles compared to co-incubation of nanoparticles and microbubbles, *Pharmaceutics*, 2021, **13**(5), 640.
19 L. Meng, X. Liu, Y. Wang, W. Zhang, W. Zhou and F. Cai, *et al.*, Sonoporation of Cells by a Parallel Stable Cavitation Microbubble Array, *Adv. Sci.*, 2019, **6**(17), 1900557.
20 S. Lee, H. Han, H. Koo, J. H. Na, H. Y. Yoon and K. E. Lee, *et al.*, Extracellular matrix remodeling in vivo for enhancing tumor-targeting efficiency of nanoparticle drug carriers using the pulsed high intensity focused ultrasound, *J. Controlled Release*, 2017, **263**, 68–78.
21 A. R. Rezk, H. Ahmed, S. Ramesan and L. Y. Yeo, High Frequency Sonoprocessing: A New Field of Cavitation-Free Acoustic Materials Synthesis, Processing, and Manipulation, *Adv. Sci.*, 2021, **8**(1), 2001983.
22 K. Entzian and A. Aigner, Drug delivery by ultrasound-responsive nanocarriers for cancer treatment, *Pharmaceutics*, 2021, **13**(8), 1–31.
23 A. Jain, A. Tiwari, A. Verma and S. K. Jain, Ultrasound-based triggered drug delivery to tumors, *Drug Delivery Transl. Res.*, 2018, **8**, 150–164.

24 I. De Cock, G. Lajoinie, M. Versluis, S. C. De Smedt and I. Lentacker, Sonoprinting and the importance of microbubble loading for the ultrasound mediated cellular delivery of nanoparticles, *Biomaterials*, 2016, **83**, 294–307.

25 M. D. Bourn, D. V. B. B. Batchelor, N. Ingram, J. R. McLaughlan, P. L. Coletta and S. D. Evans, *et al.*, High-throughput microfluidics for evaluating microbubble enhanced delivery of cancer therapeutics in spheroid cultures, *J. Controlled Release*, 2020, **326**, 13–24.

26 C. Bing, Y. Hong, C. Hernandez, M. Rich, B. Cheng and I. Munaweera, *et al.*, Characterization of different bubble formulations for blood-brain barrier opening using a focused ultrasound system with acoustic feedback control, *Sci. Rep.*, 2018, **8**(1), 1–12.

27 S. Roovers, J. Deprez, D. Priwitaningrum, G. Lajoinie, N. Rivron and H. Declercq, *et al.*, Sonoprinting liposomes on tumor spheroids by microbubbles and ultrasound, *J. Controlled Release*, 2019, **316**, 79–92.

28 S. Ramesan, A. R. Rezk, C. Dekiwadia, C. Cortez-Jugo and L. Y. Yeo, Acoustically-mediated intracellular delivery, *Nanoscale*, 2018, **10**(27), 13165–13178.

29 S. Ramesan, A. R. Rezk, P. M. Cevaal, C. Cortez-Jugo, J. Symons and L. Y. Yeo, Acoustofection: High-Frequency Vibrational Membrane Permeabilization for Intracellular siRNA Delivery into Nonadherent Cells, *ACS Appl. Bio Mater.*, 2021, **4**(3), 2781–2789.

30 H. Li, J. R. Friend and L. Y. Yeo, Surface acoustic wave concentration of particle and bioparticle suspensions.

31 R. Habibi and A. Neild, Sound wave activated nano-sieve (SWANS) for enrichment of nanoparticles, *Lab Chip*, 2019, **19**(18), 3032–3044.

32 C. Eckart, Vortices and Streams Caused by Sound Waves, *Phys. Rev.*, 1948, **73**(1), 68–76.

33 R. Habibi and A. Neild, Sound wave activated nano-sieve (SWANS) for enrichment of nanoparticles, *Lab Chip*, 2019, **19**(18), 3032–3044.

34 R. Habibi, V. He, S. Ghavamian, A. de Marco, T.-H. Lee and M.-I. Aguilar, *et al.*, Exosome trapping and enrichment using a sound wave activated nano-sieve (SWANS), *Lab Chip*, 2020, **20**(19), 3633–3643.

35 R. Mettin, I. Akhatov, U. Parlitz, C. Ohl and W. Lauterborn, Bjerknes forces between small cavitation bubbles in a strong acoustic field, *Phys. Rev. E: Stat. Phys., Plasmas, Fluids, Relat. Interdiscip. Top.*, 1997, **56**(3), 2924–2931.

36 B. Ihnatsenka and A. P. Boezaart, Ultrasound: Basic understanding and learning the language, *Int. J. Shoulder Surg.*, 2010, **4**(3), 55–62.

37 M. Wiklund, R. Green and M. Ohlin, Acoustofluidics 14: Applications of acoustic streaming in microfluidic devices, *Lab Chip*, 2012, **12**(14), 2438–2451.

38 G. Destgeer, H. Cho, B. H. Ha, J. H. Jung, J. Park and H. J. Sung, Acoustofluidic particle manipulation inside a sessile droplet: four distinct regimes of particle concentration, *Lab Chip*, 2016, **16**(4), 660–667.

39 G. Destgeer, H. B. Hang, J. Park, J. J. Ho, A. Alazzam and S. H. Jin, Microchannel Anechoic Corner for Size-Selective Separation and Medium Exchange via Traveling Surface Acoustic Waves, *Anal. Chem.*, 2015, **87**, 37.

40 R. J. Shilton, M. Travagliati, F. Beltram and M. Cecchini, Microfluidic pumping through miniaturized channels driven by ultra-high frequency surface acoustic waves, *Appl. Phys. Lett.*, 2014, **105**(7), 074106.

41 G. Destgeer, B. H. Ha, J. Park, J. H. Jung, A. Alazzam and H. J. Sung, Travelling Surface Acoustic Waves Microfluidics, *Phys. Procedia*, 2015, **70**, 34–37.

42 A. Fakhfouri, C. Devendran, D. J. J. Collins, Y. Ai and A. Neild, Virtual membrane for filtration of particles using surface acoustic waves (SAW), *Lab Chip*, 2016, **16**(18), 3515–3523.

43 A. V. Grayver and J. Noir, Particle streak velocimetry using ensemble convolutional neural networks, *Exp. Fluids*, 2020, **61**(2), 1–12.

44 M. H. Qureshi, W. H. Tien and Y. J. Lin, Performance comparison of particle tracking velocimetry (PTV) and particle image velocimetry (PIV) with long-exposure particle streaks, *Meas. Sci. Technol.*, 2020, **32**(2), 024008.

45 R. Zhong, S. Yang, G. S. Ugolini, T. Naquin, J. Zhang and K. Yang, *et al.*, Acoustofluidic Droplet Sorter Based on Single Phase Focused Transducers, *Small*, 2021, **17**(46), 2103848.

46 R. B. Moreira, L. Hamieh, E. Gjini, A. Lako, K. M. Krajewski and C. H. Yoon, *et al.*, Regression of multifocoal in transit melanoma metastases after palliative resection of dominant masses and 2 years after treatment with ipilimumab, *J. Immunother. Cancer.*, 2017, **5**(1), 1–4.

47 M. I. Gimbel, K. A. Delman and J. S. Zager, Therapy for unresectable recurrent and in-transit extremity melanoma, *Cancer Control*, 2008, **15**(3), 225–232.

48 A. Sargenti, F. Musmeci, C. Cavallo, M. Mazzeschi, S. Bonetti and S. Pasqua, *et al.*, A new method for the study of biophysical and morphological parameters in 3D cell cultures: Evaluation in LoVo spheroids treated with crizotinib, *PLoS One*, 2021, **16**(6), e0252907.

49 L. Alhasan, A. Qi, A. Al-Abboodi, A. Rezk, P. P. Y. Chan and C. Iliescu, *et al.*, Rapid Enhancement of Cellular Spheroid Assembly by Acoustically Driven Microcentrifugation, *ACS Biomater. Sci. Eng.*, 2016, **2**(6), 1013–1022.

50 H. Nam, H. J. Sung, J. Park and J. S. Jeon, Manipulation of cancer cells in a sessile droplet via travelling surface acoustic waves, *Lab Chip*, 2022, **22**(1), 47–56.

51 C. Rossmanna and D. Haemmerich, Review of temperature dependence of thermal properties, dielectric properties, and perfusion of biological tissues at hyperthermic and ablation temperatures, *Crit. Rev. Biomed. Eng.*, 2014, **42**(6), 467–492.

52 G. Destgeer, B. Ha, J. Park and H. J. Sung, Lamb Wave-Based Acoustic Radiation Force-Driven Particle Ring Formation Inside a Sessile Droplet, *Anal. Chem.*, 2016, **88**(7), 3976–3981.

53 M. B. Cutrona and J. C. Simpson, A High-Throughput Automated Confocal Microscopy Platform for Quantitative Phenotyping of Nanoparticle Uptake and Transport in Spheroids, *Small*, 2019, **15**(37), 1902033.

54 J. K. Barton, Dynamic Changes in Optical Properties, In: *Optical-Thermal Response of Laser-Irradiated Tissue*, Springer Netherlands, Dordrecht, 2010, pp. 321–349.
55 I. A. Khawar, T. Ghosh, J. K. Park and H. J. Kuh, Tumor spheroid-based microtumor models for preclinical evaluation of anticancer nanomedicines, *J. Pharm. Invest.*, 2021, **51**(5), 541–553.
56 E. Geervliet, S. Moreno, L. Baiamonte, R. Booijink, S. Boye and P. Wang, *et al.*, Matrix metalloproteinase-1 decorated polymersomes, a surface-active extracellular matrix therapeutic, potentiates collagen degradation and attenuates early liver fibrosis, *J. Controlled Release*, 2021, **332**, 594–607.
57 M. U. Munir, Nanomedicine Penetration to Tumor: Challenges, and Advanced Strategies to Tackle This Issue, *Cancers*, 2022, **14**(12), 2904.
58 Z. Skrott, M. Mistrik, K. K. Andersen, S. Friis, D. Majera and J. Gursky, *et al.*, Alcohol-abuse drug disulfiram targets cancer via p97 segregase adaptor NPL4, *Nature*, 2017, **552**(7684), 194–199.
59 R. A. Paun, D. C. Dumut, A. Centorame, T. Thuraisingam, M. Hajduch and M. Mistrik, *et al.*, One-Step Synthesis of Nanoliposomal Copper Diethyldithiocarbamate and Its Assessment for Cancer Therapy, *Pharmaceutics*, 2022, **14**(3), 640.
60 V. Rizzo, C. Morton, N. DePaola, J. E. Schnitzer and P. F. Davies, Recruitment of endothelial caveolae into mechanotransduction pathways by flow conditioning in vitro, *Am. J. Physiol.*, 2003, **285**(4), H1720–H1729.
61 B. Sinha, D. Köster, R. Ruez, P. Gonnord, M. Bastiani and D. Abankwa, *et al.*, Cells respond to mechanical stress by rapid disassembly of caveolae, *Cell*, 2011, **144**(3), 402–413.
62 R. G. Parton, M. M. Kozlov and N. Ariotti, Caveolae and lipid sorting: Shaping the cellular response to stress, *J. Cell Biol.*, 2020, **219**(4), e201905071.
63 A. L. Kiss and E. Botos, Endocytosis via caveolae: alternative pathway with distinct cellular compartments to avoid lysosomal degradation?, *J. Cell. Mol. Med.*, 2009, **13**(7), 1228.
64 C. Matthaeus and J. W. Taraska, Energy and Dynamics of Caveolae Trafficking, *Front. Cell Dev. Biol.*, 2021, **8**, 1842.
65 Y. Song, Y. Wu, L. Xu, T. Jiang, C. Tang and C. Yin, Caveolae-Mediated Endocytosis Drives Robust siRNA Delivery of Polymeric Nanoparticles to Macrophages, *ACS Nano*, 2021, **15**(5), 8267–8282.
66 A. Saalbach, G. Hildebrandt, U. F. Haustein and U. Anderegg, The Thy-1/Thy-1 Ligand Interaction Is Involved in Binding of Melanoma Cells to Activated Thy-1- Positive Microvascular Endothelial Cells, *Microvasc. Res.*, 2002, **64**(1), 86–93.
67 M. Brenet, S. Martínez, R. Pérez-Nuñez, L. A. Pérez, P. Contreras and J. Díaz, *et al.*, Thy-1 (CD90)-Induced Metastatic Cancer Cell Migration and Invasion Are β3 Integrin-Dependent and Involve a Ca2+/P2X7 Receptor Signaling Axis, *Front. Cell Dev. Biol.*, 2021, 8.
68 T. A. Rege and J. S. Hagood, Thy-1 as a regulator of cell-cell and cell-matrix interactions in axon regeneration, apoptosis, adhesion, migration, cancer, and fibrosis, *FASEB J.*, 2006, **20**(8), 1045–1054.
69 P. Hu and T. H. Barker, Thy-1 in Integrin Mediated Mechanotransduction, *Front. Cell Dev. Biol.*, 2019, **7**, 22.
70 C. Sauzay, K. Voutetakis, A. A. Chatziioannou, E. Chevet and T. Avril, CD90/Thy-1, a cancer-associated cell surface signaling molecule, Front Cell, *Dev. Biol.*, 2019, **7**, 66.
71 A. B. Meriin, A. Narayanan, L. Meng, I. Alexandrov, X. Varelas and I. I. Cissé, *et al.*, Hsp70–Bag3 complex is a hub for proteotoxicity-induced signaling that controls protein aggregation, *Proc. Natl. Acad. Sci.*, 2018, **115**(30), E7043–E7052.
72 B. Artegiani, D. Hendriks, J. Beumer, R. Kok, X. Zheng and I. Joore, *et al.*, Fast and efficient generation of knock-in human organoids using homology-independent CRISPR/Cas9 precision genome editing, *bioRxiv*, 2020, preprint, DOI: **10.1038/s41556- 020-0472-5**.
73 S. Y. Song, J. Hong, S. Go, S. Lim, H. S. Sohn and M. Kang, *et al.*, Interleukin-4 Gene Transfection and Spheroid Formation Potentiate Therapeutic Efficacy of Mesenchymal Stem Cells for Osteoarthritis, *Adv. Healthcare Mater.*, 2020, **9**(5), 1–12.
74 T. Endo, K. Itaka, M. Shioyama, S. Uchida and K. Kataoka, Gene transfection to spheroid culture system on micropatterned culture plate by polyplex nanomicelle: A novel platform of genetically-modified cell transplantation, *Drug Delivery Transl. Res.*, 2012, **2**(5), 398–405.
75 K. Zhang, H. Fang, Y. Qin, L. Zhang and J. Yin, Functionalized Scaffold for in Situ Efficient Gene Transfection of Mesenchymal Stem Cells Spheroids toward Chondrogenesis, *ACS Appl. Mater. Interfaces*, 2018, **10**(40), 33993–34004.
76 B. Laperrousaz, S. Porte, S. Gerbaud, V. Härmä, F. Kermarrec and V. Hourtane, *et al.*, Direct transfection of clonal organoids in Matrigel microbeads: a promising approach toward organoid-based genetic screens, *Nucleic Acids Res.*, 2018, **46**(12), e70.
77 S. Letzsch, K. Boettcher and A. Schreiner, Cellular Imaging and Analysis T E C H N I C A L N O T E Clearing Strategies for 3D Spheroids.
78 H. Hama, H. Hioki, K. Namiki, T. Hoshida, H. Kurokawa and F. Ishidate, *et al.*, ScaleS: an optical clearing palette for biological imaging, *Nat. Neurosci.*, 2015, **18**(10), 1518–1529.